Eur. Phys. J. D (2016) 70: 50
DOI: 10.1140/epjd/e2016-60564-4

THE EUROPEAN PHYSICAL JOURNAL D

Regular Article

Effect of geometrical focusing on femtosecond laser filamentation with low pressure

Haitao Wang[1,2,a], Wei Jia[3], and Chengyu Fan[1]

[1] Key Laboratory of Atmospheric Composition and Optical Radiation, Anhui Institute of Optics and Fine Mechanics, Chinese Academy of Sciences, Hefei Anhui 230031, P.R. China
[2] State Key Laboratory of Pulsed Power Laser Technology, Electronic Engineering Institute, Hefei 230037, P.R. China
[3] College of Mechanical and Electrical Engineering, Anhui Jianzhu University, Hefei Anhui 230031, P.R. China

Received 7 October 2015 / Received in final form 29 November 2015
Published online 10 March 2016 –

Abstract. The influence of geometrical focusing on the filamentation of femtosecond laser pulses at various low pressures (<1 atm) in air has been numerically demonstrated. The main peculiarities, such as filamentation dynamics, spatial-temporal evolution and supercontinuum generation manipulated by external geometrical focusing in the low atmospheric pressure regime, are analyzed by numerically solving a spatial-temporal equation for femtosecond laser pulse propagation in air. The results show that those important characteristics are more sensitive to the focal length than the variation of atmospheric pressure. It indicates that suitable design of the focal length will result in further amplitude uniformity and a lack of temporal aberrations in the compressed pulse. This theoretical modelling of pulse shaping optimization is a step to realization of high-energy femtosecond pulse delivery from the Earth's surface to altitudes of several kilometers up into the atmosphere.

1 Introduction

Propagation of ultra-short laser pulses in transparent media have attracted more and more interest both in experimental and theoretical researches in the last several years [1–3]. For an incident laser pulse whose peak power exceeds the critical power (P_{cr}) of self-focusing, a filamentary propagation configuration can be formed. The filamentation phenomenon is a dynamical process associated with a competition between several physical mechanisms; the major effects are Kerr self-focusing, diffraction and laser-induced optical photon ionization. The combined action of those effects can maintain high intensity ($10^{13} \sim 10^{14}$ W/cm^2) confined within a narrow channel over a long distance [4–6]. Femtosecond filamentation is a special aspect related to the issue of light filament propagation, due to the promising advantages of filamentation for THz radiation [7], triggering and guiding [8], attosecond and supercontinuum generation [9], remote sensing [10], lasing action [11,12] and laser-assisted condensation [13–15].

A wide range of filamentary applications [16–19] based on the driven force of laser filamentation are dependent on the stability and effective interaction length of the filament. It is possible to control the filament formation by changing the parameters of femtosecond laser pulses (powers and durations) and spatial and temporal characteristics. It has been reported that controllable filament can be achieved over horizontal and vertical kilometric distances by changing the chirp of the incident pulse [4,20]. For outdoor large-scale lighting control and LIDAR applications at high altitude (low pressure), the impact of pressure is not an ignorable parameter on the prefocused laser pulse filamentation process in the ambient atmosphere. It has been numerically shown that the existence of low pressure filamentary paradigms, as well as the prolonged length of the plasma channels at various pressures from 0.1 to 1 atm (1 atm $\sim 10^5$ Pa), which correspond to vertical attitudes higher than 10 km [6,21]. In laboratory-scale methods, which are conducted in pressurized gas cells [22,23], the excitation of plasma can be well controlled by changing the gas pressure to obtain filament applications, such as pulse shortening and high harmonic generation. In low pressure conditions, the plasma generation is suppressed due to the decrease of neutral gas molecule density weakening photo-ionization. In contrast to this scenario, the plasma density variation is tremendously dependent on external focusing [24]. Its maximum magnitude can be progressively increases, attributed to the shortening of focus length. The spatial characterizations of focused filamentation at low pressure have been extensively investigated [1,2,6,25]. However, it is still an open question about how the focus lens affects the temporal evolution and spectrum dynamics of the plasma channel when pressure dependency becomes less pronounced.

[a] e-mail: htwang@aiofm.ac.cn

In this paper, we numerically investigated the influence of focus lens on the filamentation of femtosecond laser pulses in various low pressures (<1 atm) in air. The motivation for undertaking this study is to investigate the combination role of focus lens and low pressure in the filamentation process; furthermore, to identify and elucidate the different temporal evolution and spectrum dynamics of the plasma channel in the regimes of nonlinear pulse propagation.

2 The physical model

Maxwell's equations as the standard mathematical model governing the evolution of an electromagnetic field propagation through a dielectric medium can be expressed as a set of coupled vector-wave equations containing the electric field **E**, the dielectric displacement field **D** and the current density **J**. For a practical scalar version, the Unidirectional Pulse Propagation Equations (UPPE) are exact system of equations that describe evolution of ultra-short laser pulses along the positive z-direction for the forward propagating field. The canonical model of the equations in the spectral domain can be read [26,27]:

$$\frac{\partial \hat{E}(r,z,\omega)}{\partial z} = \left(\frac{i}{2k(\omega)}\nabla_{\perp}^{2} + ik(\omega)\right)\hat{E}(r,z,\omega) + \frac{i\omega^{2}}{2k(\omega)c^{2}\varepsilon_{0}}\left(\hat{P}_{NL}(r,z,\omega) + i\frac{\hat{J}(r,z,\omega)}{\omega}\right). \quad (1)$$

In this equation, the four terms on the right-hand side correspond to diffraction, dispersion, SPM, and plasma behavior, respectively. $\hat{E}(r,z,\omega)$ represents the Fourier presentation of the forward propagation electric field component, $k(\omega) = n(\omega)\omega/c$ is the wave vector and $n(\omega)$ is the linear refractive index of the material, c and ω are light speed and the optical frequency, respectively. $\hat{P}_{NL}(r,z,\omega)$ accounts for the nonlinear polarization in the frequency domain of $P_{NL}(r,z,t) = 2\varepsilon_0 n_0 n_2 I(r,z,t)E(r,z,t)$ in the space-time domain; n_0, n_2 are the linear refractive index and nonlinear coefficient at center wavelength λ_0, and ε_0 denotes the permittivity of free space. Taking into account the generation of plasma and the photoionization losses, the current density $J(r,z,t) = J_P(r,z,t) + J_{PI}(r,z,t)$. In the frequency domain, the free carrier current density by photoionization is treated in terms of a Drude model [1,2] according to the equation:

$$\hat{J}_P(r,z,\omega) = c^2\varepsilon_0\left(\frac{n_0\sigma(\omega)}{c} + i\frac{\omega_0^2}{c^2\rho_c\omega(1+\nu_e^2/\omega^2)}\right) \times \left(\hat{\rho}(r,z,\omega)\otimes\hat{E}(r,z,\omega)\right)$$

and the loss current is

$$J_{PI}(r,z,t) = \frac{k_0c^2\varepsilon_0}{\omega_0}\frac{U_iW(I)}{I(r,z,t)}\{\rho_0 - \rho(r,z,t)\}E(r,z,t),$$

where $\nu_e = 1/\tau_c$ and $\rho_c = \omega_0^2 m_e\varepsilon_0/q_e^2$ is the critical plasma density above which the plasma becomes opaque ($\rho_c = 1.8\times10^{21}$ cm^{-3} at $\lambda_0 = 800$ nm); here, q_e and $m_e$denote electron charge and mass, respectively, and τ_c represents the electron collision time. The cross-section for inverse Bremsstrahlung also follows the Drude model and is given by $\sigma(\omega) = k_0\omega\tau_c/n_0^2\rho_c(1+\omega^2\tau_c^2)$. The self-generated plasma density $\rho(r,z,t)$ satisfies the rate equation [1,2]:

$$\frac{\partial\rho(r,z,t)}{\partial t} = W(I)\{\rho_0 - \rho(r,z,t)\} + \frac{\sigma(\omega_0)}{U_i}\rho(r,z,t)|E(r,z,t)|^2, \quad (2)$$

where the quantity U_i and ρ_0 denote the molecules ionization potential in air and the neutral gas density, respectively. The multi-photon ionization (MPI) rate obeys the results of the Perelomov-Popov-Terent'ev (PPT) ionization model and can be approximately expressed by $W(|E(r,z,t)|^2) \to W_{MPI} = \sigma_K|E(r,z,t)|^{2K}$, σ_K denotes the photoionization cross section and $K = \mathrm{mod}(U_i/\hbar\omega_0 + 1)$ is the minimum number of photons necessary to ionize the gas medium and its quantity depends on the gas species. Because most of the pulse energy is converged right around the central frequency, we approximately adopt $\sigma(\omega) \approx \sigma(\omega_0)$ to simplify the calculation of the contribution from avalanche ionization.

The input laser pulses are with Gaussian profiles both in the spatial and temporal domain as follows:

$$E(r,t,z=0) = \sqrt{\frac{2P_{in}}{\pi r_0^2}}\exp\left\{-\frac{r^2}{r_0^2}\right\} \times \frac{1}{2\pi}\int_{-\infty}^{\infty}d\omega\exp\left(i\frac{(\omega+\omega_0)r^2}{2cf} + i\omega t\right) \times \Im\left[\exp\left(-\frac{t^2}{T_p^2}\right)\right], \quad (3)$$

where

$$\Im[E(t)] = \int_{-\infty}^{\infty}dt\exp\left(-\frac{t^2}{T_p^2}\right)\exp(-i\omega t)$$

represents the Fourier transform of the temporal profile of the input pulse. Equation (3) includes the importance of a frequency dependent lens factor [28] describing the fact that different frequency components of the input pulse have different wavefront curvature and will be diffracted into different cone angles. In the calculation, $P_{in} = 2.1P_{cr}$, $r_0 = 1.0$ mm, $T_p = 30$ fs, and f denote input pulse peak power, beam radius, pulse duration, and effective focal length, respectively. $k_0 = \omega_0/c = 2\pi n_0/\lambda_0$ and ω_0 are the wave number and the angular frequency of the carrier wave, respectively. We use the full-width at half maximum (FWHM) $t_{\mathrm{FWHM}} = \sqrt{2\ln 2}T_p$ with respect to the intensity and introduce the pulse energy through $E_{in} = P_{in}T_p\sqrt{\pi/2}$ to characterize the incident pulses.

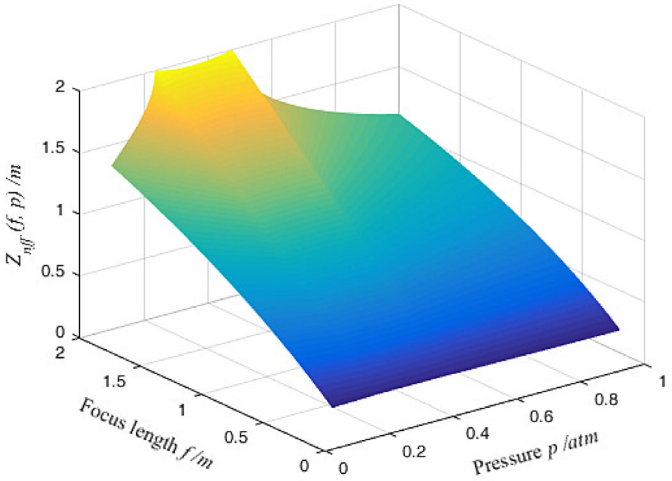

Fig. 1. 3D plot of the nonlinear focus position as a function of both the parameter variables of focus length f and atmospheric pressure p.

Under the consideration the variation of the gaseous medium pressure p, which is expressed in atm, the parametric values of the above equation coefficients vary as follows [21,22]:

$$\begin{aligned} n_2 &= n_{2,0} \times p, \quad \tau_c = \tau_{c,0}/p, \\ \sigma &= \sigma_0 \times p \times \left(1 + \omega_0^2 \tau_{c,0}^2\right) / \left(p^2 + \omega_0^2 \tau_{c,0}^2\right), \\ \rho_{at} &= \rho_{at,0} \times p, \beta_K = \beta_{K,0} \times p. \end{aligned} \tag{4}$$

Here, the index 0 denotes the initial values of the parameters at atmosphere pressure 1 atm.

3 Results and discussion

We are interested in the situation where an initial collimated Gaussian beam is focused by a lens of focal length f at different pressures p. The longitudinal focus position of the input Gaussian beam under conditions of linear focusing is determined by: $z_{lf} = f/\left(1 + f^2/z_R^2\right)$, here $z_R = \pi n_0 r_0^2/\lambda_0$ denotes the Rayleigh range (diffraction length) of the input laser beam. A collimated beam with peak power several times above the self-focusing threshold will collapse to a singularity at $z_{nf} = 0.367 z_R/\sqrt{\left[p_{in}/p_{cr}(p) - 0.852\right]^2 - 0.0219}$, if there exists no other saturation mechanism to counterbalance Kerr nonlinear effect [1,2]. By considering the effect of the focus lens, the shifting of focus position due to Kerr nonlinear focusing can be expressed as $\Delta z_{fShift} = z_{nff} - z_{lf}$, here $z_{nff} = 0.367 z_R/(\sqrt{\left[p_{in}/p_{cr}(p) - 0.852\right]^2 - 0.0219} + 0.367 z_R/f)$ denotes the collapse distance of a focused Gaussian beam. In the considered pressure range ($p <$ 1 atm), the nonlinear focus positions and their shifting are displayed in Figure 1. The nonlinear focus positions become closer to the laser source and the focus shift becomes smaller, with the reducing of focal lengths and pressures. At the first formation stage of focus position with low pressures, the self-focusing becomes less important because of the divergence of critical power of self-focusing, similarly for group velocity dispersion (GVD) as characterized by $k'' \sim p$ and MPI with threshold mechanism denoted by equation (4). The focus lens becomes important and dominates for the resulting focus shift. Indeed, the plasma generation as the defocusing effect also contributes to the focus position shift, despite it being a minimal factor. In contrast, in the intermediate ($p > 1$ atm) and high-pressure regimes ($p \gg 1$ atm) [29], other effects, such as GVD, MPI and self-focusing, are dominant at the stage of first focus formation and in the filamentation dynamics beyond the focus point. This is why we firstly analyse the focus shifting at the self-focusing stage. In the next section, we mainly focus on the filamentation dynamics beyond the focus point at low pressures.

A single filament is formed for the input peak power slightly higher than the critical power of self-focusing. For the fixed incident peak power, stabilization propagation with intensity clamping [30,31] can be observed for three types of focal lengths at different pressures. The clamping intensities [32] for various pressures are comparable, but slight differences are obtained depending on the external focus cases. When the focus becomes tighter, it results in higher peak intensity as well as plasma density as shown in the buttom row of Figure 2. Those observations are consistent with the actual demonstrations that a little change in intensity would lead to a huge change in the plasma density (i.e., by two or three orders of magnitude) with geometrical focusing [24]. With the reducing of the pressure, the longer the filament length and the broader the filament diameter associated with the full width at half maximum (FWHM) of the spatial distribution of the fluence $F(r,z) = \int_{-\infty}^{+\infty} I(r,z,\tau)\, d\tau$. Those configurations have been observed in the previous studies [6]. The difference is that we don't think the longer filament length and broader diameter is due to the variation of local plasma density. In our cases, under a given focus condition, the plasma densities are comparable for various pressures. The identical plasma peak density is due to nearly the same peak intensity, which is independent of the pressure and remains constant in the filament. It can be simply explained that at lower pressure the energy losses due to MPI ($\beta_K \sim p$) and plasma absorption ($\sigma \sim p$) are decreased as can be seen from formula (4). It indicates that at lower pressure the beam can preserve more energy (power) subsistence to sustain the longer propagation. For the same focus length, higher pressure leads to the energy losses due to MPI and plasma absorption are increased, those energy losses will inevitably prolong the nonlinear focus point along the propagation axis. It has been theoretical predicted that in the transverse cross section ($r_\perp$) of a single filament attaining the saturation level $2p_{fil}/\pi r_\perp^2 \to I_{\max}$, the conveying power of the filament in air can be estimated by $p_{fil} \cong \pi^2 p_{cr}/4 < 7p_{cr}$ [33], which is slightly higher than the value estimated by using $p_{fil} \cong \pi^2 p_{cr}/2 < 12.5 p_{cr}$ [34]. Then, the filament diameter variation as a function of pressure can be expressed as $I_{\max} \pi r_\perp^2 \sim p_{cr}(p) \sim 1/p$ [35]. This is in agreement with

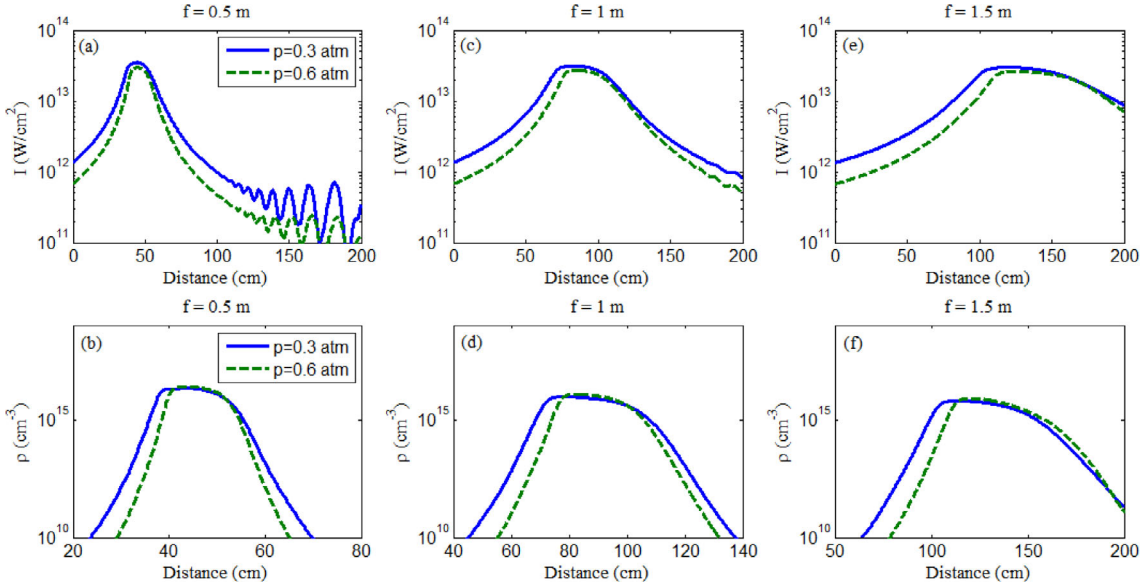

Fig. 2. The on-axis peak intensity and plasma density as a function of propagation distance. (a) and (b): $f = 0.5$ m; (c) and (d): $f = 1.0$ m; (e) and (f): $f = 1.5$ m. The blue solid line represents $p = 0.3$ atm and the cyan dash line is $p = 0.6$ atm.

the previous study [6,21]. The on-axis intensity maximum remains constant independent of the pressure, the inverse proportion relationships between the width of the filament channel and atmospheric pressure indicates that the filament becomes broader with reducing of the pressure. At the same time, all the results from reducing pressure will be enhanced with decreasing of the focal length. The numerical results are stable with respect to the chosen initial condition in the sense that if the total pulse power is kept constant, then changing the external focus geometry not only changes the onset of the filament but also its important characteristics, such as filament length, peak intensity and the generated plasma density, as seen in Figure 2.

At low pressures, self-focusing is not so significantly important as it becomes in high pressures for the temporal evolution of the propagating laser pulse. In contrast, plasma-induced self-phase modulation (PI-SPM) and defocusing effects associated with the factor $\sigma\omega\tau_c$ become substantial contributors and dominate The PI-SPM involves the electron collision rate τ_c which increases with decreasing pressure in a longer plasma channel with a wider diameter and only plays an important role at the trailing part of the pulse. Then its contributing to the reshaping of the pulse trail becomes weak and slows down. As a result, the temporal profiles are more homogeneous and symmetrical at 0.3 atm (the left column in Fig. 3) than that at 0.6 atm (the right column in Fig. 3). At tight focus geometry (i.e., $f = 0.5$ m), the self-steepen and spatial-temporal focusings are reinforced, resulting in dramatic temporal compressing and reshaping of the pulse seen in Figures 3a and 3b. As the pulse propagates, a second self-focusing cycle develops and reforms, at a further propagation distance, on the trailing edge of the pulse due to dynamic spatial replenishment [36]. In contrast, at intermediate focus geometry, the plasma defocusing at the trail of the pulse has been weakened compared with the case at tight focusing. The back part of the pulse can survive for a slightly long propagation distance, but it is gradually diffracted into the background field ultimately (Figs. 3c and 3d). At this condition, the temporal profile $f(t)$ in the filamentation regime is most homogenous due to the pulse splitting corresponding with GVD is not significant. With further weakening of the focus lens, i.e., $f = 1.5$ m, the filamentation length is the longest and the filament diameter is the largest compared with the other two cases (not shown here). It suggests that at this situation the nonlinear interactions (length and range) are the strongest. As a result, the pulse profile is tremendously deteriorated along the filamentary pulse propagating direction (Figs. 3e and 3f). The longest filamentation configuration formation is at the costs of symmetry deterioration and loss of uniformity of the pulse.

The temporal asymmetries also associated with spectrum asymmetries as presented in Figure 3. The spectra are relatively homogeneous and symmetric at 0.3 atm compared to those at 0.6 atm. In the process of filamentation and pulse self-compressing [37,38], Kerr self-phase modulation (K-SPM) produces a frequency chirp across the pulse and then pushes apart the two oppositely frequency-shifted halves towards both-sides of the pulse [39]. The considerable spectrum broadening on the infrared pedestal side is mainly generated from K-SPM producing a negative frequency chirp manifested by $\Delta\omega = -\omega_0 n_2 z \partial I/c\partial t < 0$ in the leading of the pulse [25] High pressure ($n_2 \sim p$) and tight geometric focusing (reinforcing the slop of intensity) are positive contributions to K-SPM, which eventually lead to negative red-shift spectrum broadening. In contrast, it is well known that in a filament, the plasma generation is significant only in the trail of the pulse. The noticeable ultraviolet (UV) spectrum broadening corresponding to the frequency blue shift $\Delta\omega = +2\pi z e^2 \partial\rho/cm_e\omega_0\partial t$, is attributed to PI-SPM.

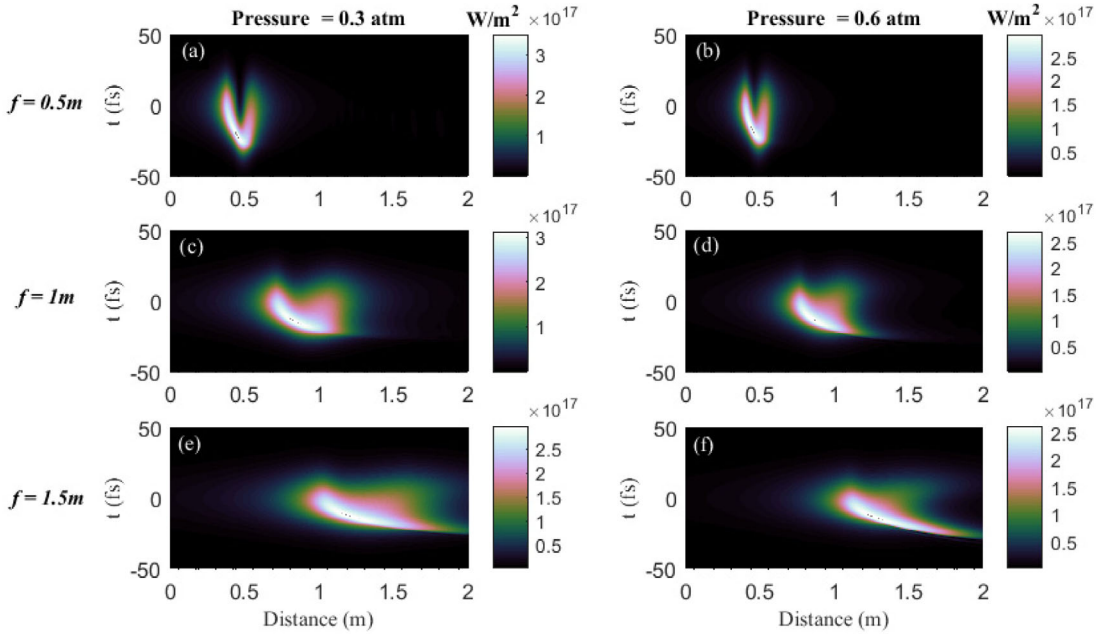

Fig. 3. Spatial-temporal dynamics of femtosecond filamentation in air at different pressures and different focus geometries. (a) and (b): $f = 0.5$ m; (c) and (d): $f = 1.0$ m; (e) and (f): $f = 1.5$ m.

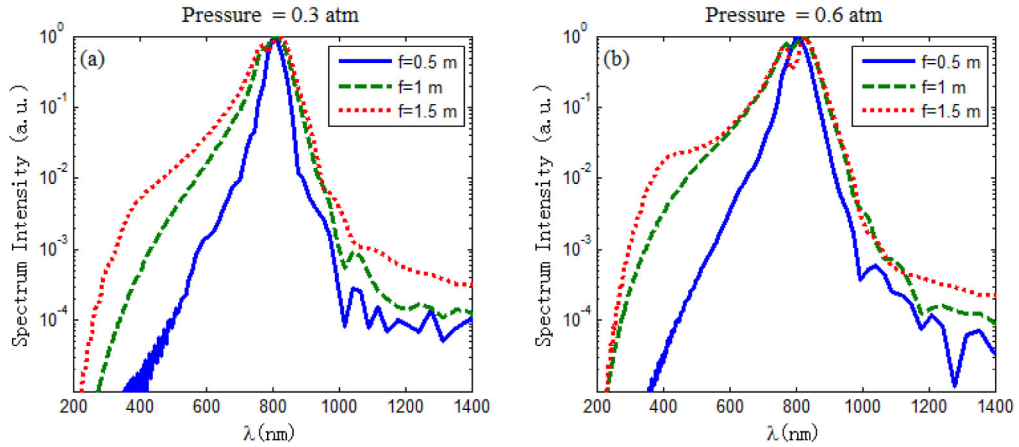

Fig. 4. The corresponding normalized superbroadened spectral intensity distributions of the pulses at $z = 2$ m for two different pressures under three fixed chosen geometries $f = 0.5$ m (blue solid line); $f = 1.0$ m (cyan dash line) and $f = 1.5$ m (red dot line).

It differs from the spectrum broadening conducted in argon in the pressure range above 1 atm in the earlier study [29] In our case, the plasma is mainly generated by MPI (the first term in formula (2)) of air (and oxygen) molecules combining the action of self-steepening as well as time-space focusing effect, resulting in abnormal swelling near the second harmonic position in the UV spectrum side, eventually leading to self-compressed few-cycle shocked waves [40] especially for high pressure and large geometrical focusing as shown in Figure 4. The broadened spectrum in the blue side is formed due to the additional phase modulation, in addition to plasma generation, during the falling edge of the filamenting pulse with low pressure [22]. Further shortening of the geometrical focusing means reduced nonlinear interaction length and narrowed spectral extension range.

4 Summary

In the actual applications of femtosecond laser filamentation in air [41], it is difficult to deliver high energy laser pulses at kilometric heights or depths along a vertical axis without using a focus lens. We have physically and numerically demonstrated the influence of geometrical focusing on the filamentation of femtosecond laser pulses in various low pressures (<1 atm) in air. The important characteristics, such as onset position, filament length, peak intensity and the generated plasma density, are more sensitive to the focal length rather than the variation of atmospheric pressure. Geometrical focusing is also a significant role in the temporal and spectral structure evolution. It indicates that the suitable design of the focal length will result in further amplitude uniformity and the lack of temporal

aberrations in the compressed pulse. This theoretical modelling of pulse shaping optimization is a step to realization of the high-energy femtosecond pulse delivery from the ground surface to several kilometer altitudes up in the atmosphere. This work may offer significant advantages in numerous fields such as the controllable super-continuum generation or remote sensing techniques.

The project was supported by the Open Research Fund of State Key Laboratory of Pulsed Power Laser Technology, Electronic Engineering Institute (Grant Nos. SKL2013KF01, SKL2015KF03).

References

1. A. Couairon, A. Mysyrowicz, Phys. Rep. **441**, 47 (2007)
2. L. Bergé, S. Skupin, R. Nuter, J. Kasparian, J.P. Wolf, Rep. prog. phys. **70**, 1633 (2007)
3. S.L. Chin, T.J. Wang, C. Marceau, J. Wu, J.S. Liu, O. Kosareva, N. Panov, Y.P. Chen, J.F. Daigle, S. Yuan, A. Azarm, W.W. Liu, T. Seideman, H.P. Zeng, M. Richardson, R. Li, Z.Z. Xu, Laser Phys. **22**, 1 (2012)
4. J. Kasparian, M. Rodriguez, G. Méjean, J. Yu, E. Salmon, H. Wille, R. Bourayou, S. Frey, Y.B. André, A. Mysyrowicz, R. Sauerbrey, J.P. Wolf, L. Wöste, Science **301**, 61 (2003)
5. M. Durand et al., Opt. Express **21**, 26836 (2013)
6. S. Hosseini, O. Kosareva, N. Panov, V.P. Kandidov, A. Azarm, J.-F. Daigle, A.B. Savelév, T.-J. Wang, S.L. Chin, Laser Phys. Lett. **9**, 868 (2012)
7. L. Bergé, S. Skupin, C. Köhler, I. Babushkin, J. Herrmann, Phys. Rev. Lett. **110**, 073901, 2013
8. B. Forestier, A. Houard, I. Revel, M. Durand, Y.B. André, B. Prade, A. Jarnac, J. Carbonnel, M. Le Nevé, J.C. de Miscault, B. Esmiller, D. Chapuis, A. Mysyrowicz, AIP Adv. **2** 012151 (2012)
9. M. Bradler, C. Homann, E. Riedle, Appl. Phys. B **113**, 19 (2013)
10. M. Petrarca, S. Henin, N. Berti, M. Matthews, Appl. Phys. B **114**, 319 (2014)
11. T.-J. Wang, J.F. Daigle, J.J. Ju, S. Yuan, R.X. Li, S.L. Chin, Phys. Rev. A **88**, 053429 (2013)
12. H.S. Zhang, C.R. Jing, J.P. Yao, G.H. Li, B. Zeng, W. Chu, J.L. Ni, H.Q. Xie, H.L. Xu, S.L. Chin, K. Yamanouchi, Y. Cheng, Z.Z. Xu, Phys. Rev. X **3**, 041009 (2013)
13. P. Rohwetter, et al., Nat. Photon. **4**, 451 (2010)
14. J.J. Ju, J.S. Liu, C. Wang, H.Y. Sun, W.T. Wang, X.C. Ge, C. Li, S.L. Chin, R.X. Li, Z. Z Xu, Opt. Lett. **37**, 1214 (2012)
15. H. Saathoff, S. Henin, K. Stelmaszczyk, M. Petrarca, R. Delagrange, Z. Hao, J. Lüder, O. Möhler, Y. Petit, P. Rohwetter, M. Schnaiter, J. Kasparian, T. Leisner, J.P. Wolf, L. Wöste, Atmos. Chem. Phys. **13**, 4593 (2013)
16. J.-M. Manceau, M. Massaouti, S. Tzortzakis, Opt. Lett. **35**, 2424 (2010)
17. D. Dimitrovski, J. Maurer, H. Stapelfeldt, L.B. Madsen, Phys. Rev. Lett. **113**, 103005 (2014)
18. P. Béjot, G. Karras, F. Billard, E. Hertz, B. Lavorel, E. Cormier, O. Faucher, Phys. Rev. Lett. **112**, 203902 (2014)
19. N. Jhajj, E.W. Rosenthal, R. Birnbaum, J.K. Wahlstrand, H.M. Milchberg, Phys. Rev. X **4**, 011027 (2014)
20. R. Nuter, S. Skupin, L. Bergé, Opt. Lett **30**, 917 (2005)
21. A. Couairon, M. Franco, G. Méchain, T. Olivier, B. Prade, A. Mysyrowicz, Opt. Commun. **259**, 265 (2006)
22. S. Champeaux, L. Bergé, Phys. Rew. E. **68**, 066603 (2003)
23. G. Méchain, T. Olivier, M. Franco, A. Couairon, B. Prade, A. Mysyrowicz, Opt. Commun. **261**, 322 (2006)
24. F. Théberge, W. Liu, P. Tr. Simard, A. Becke, S.L. Chin, Phys. Rev. E **74**, 036406 (2006)
25. S.L. Chin, Femtosecond Laser Filamentation, *Monography, Springer series on Atomic, Optical, and Plasma Physics* (Springer Sci. Business Media, New York, 2010), Vol. 55
26. M. Kolesik, J.V. Moloney, Phys. Rev. E **70**, 036604 (2004)
27. A. Couairon, E. Brambilla, T. Corti, D. Majus, O. de J. Ramírez-Góngora, M. Kolesik, Eur. Phys. J. Special Top. **199**, 5 (2011)
28. L. Bergé, S. Skupin, G. Steinmeyer, Phys. Rev. A **79**, 033838 (2009)
29. M. Mlejnek, E.M. Wright, J.V. Moloney, Phys. Rev. E **58**, 4903 (1998)
30. S. Xu, J. Bernhardt, M. Sharifi, W. Liu, S.L. Chin, Laser Phys. **22**, 195 (2012)
31. W. Liu, Chin. J. Phys. **52**, 465 (2014)
32. J. Kasparian, R. Sauerbrey, S.L. Chin, Appl. Phys. B **71**, 877 (2000)
33. L. Bergé, S. Skupin, F. Lederer, G. Mejean, J. Yu, J. Kasparian, E. Salmon, J.-P. Wolf, M. Rodriguez, L. Wöste, R. Bourayou, R. Sauerbrey, Phys. Rev. Lett. **92**, 225002 (2004)
34. S. Tzortzakis, L. Bergé, A. Couairon, M. Franco, B. Prade, A. Mysyrowicz, Phys. Rev. Lett. **86**, 5470 (2001)
35. S. Champeaux, L. Bergé, Opt. Lett. **31**, 1301 (2006)
36. M. Mlejnek, E.M. Wright, J.V. Moloney, Opt. Lett. **23**, 382 (1998)
37. A. Mysyrowicz, A. Couairon, U. Keller, New J. Phys. **10**, 025023 (2008)
38. O.G. Kosareva, N.A. Panov, D.S. Uryupina, M.V. Kurilova, A.V. Mazhorova, A.B. Savel'ev, R.V. Volkov, V.P. Kandidov, S.L. Chin, Appl. Phys. B **91**, 35 (2008)
39. N. Aközbek, M. Scalora, C.M. Bowden, S.L. Chin, Opt. Commun. **191**, 353 (2001)
40. P.A. Zhokhov, A.M. Zheltikov, **110**, 183903 (2013)
41. P. Sprangle, J.R. Peñano, B. Hafizi, Phys. Rev. E **66**, 046418 (2002)